

CT Imaging with Helium and Carbon Ions for Hadron Radiotherapy

Zsófia Jólesz^{1,2}, Gábor Bíró¹, Gábor Papp² and Gergely Gábor Barnaföldi¹

for the Bergen pCT collaboration

¹HUN-REN Wigner Research Centre for Physics, 29–33 Konkoly–Thege Miklós út, H-1121 Budapest, Hungary

²Eötvös Loránd University, Institute of Physics and Astronomy, 1/A Pázmány Péter Sétány, H-1117 Budapest, Hungary

Abstract.

Objective: To perform a comprehensive comparative analysis of proton, helium-ion, and carbon-ion computed tomography (CT) as direct imaging modalities for hadron therapy treatment planning, focusing on Relative Stopping Power (RSP) reconstruction accuracy and patient radiation dose.

Approach: High-fidelity Monte Carlo simulations were conducted using the GATE/Geant4 platform to model a standard CTP404 phantom. RSP maps were reconstructed using an iterative Richardson-Lucy deconvolution algorithm. Imaging performance was evaluated by comparing reconstructed RSP values against ground truth data for various tissue-equivalent inserts, while integral doses were estimated for a human head geometry.

Main results: All investigated particle modalities demonstrated a significant dose reduction compared to conventional X-ray CT protocols (which are approximately 40 mGy). The estimated imaging doses were 1.6 mGy for protons, 3.9 mGy for helium ions, and 22.7 mGy for carbon ions. In terms of accuracy, carbon-ion imaging achieved the highest fidelity for soft-tissue materials (mean absolute error < 0.5%). Helium ions offered a balanced performance with sub-1% errors for most materials and a dose burden significantly lower than carbon ions. Protons exhibited the widest range of RSP deviations (−1.8% to +3.1%).

Significance: Direct particle imaging eliminates the systematic uncertainties inherent in photon-to-hadron conversion. While carbon ions provide superior RSP reconstruction precision essential for complex treatment plans in heterogeneous anatomy, helium and proton imaging offer exceptional dose sparing, making them particularly advantageous for pediatric patients and frequent adaptive replanning scenarios.

Keywords: particle computed tomography, hadron therapy, relative stopping power, Monte Carlo simulation, dosimetry, carbon ion therapy

1. Introduction

1.1. Hadron Therapy

Since cancer remains one of the leading causes of mortality worldwide, the optimization of cancer treatment continues to be an area of intense scientific investigation and has undergone substantial development over recent decades. Among the principal modalities of cancer therapy is radiotherapy, the overarching objective of which is to irradiate malignant tissue as accurately as possible while minimizing radiation exposure to surrounding healthy organs. A rapidly advancing branch of radiotherapy involves the use of hadrons (e.g. protons or heavier ions such as helium or carbon), which exhibit particularly advantageous physical properties for oncological applications due to their characteristic energy deposition profile, described by the Bragg curve (Bragg et al., 1904). This phenomenon enables highly localized dose delivery, allowing the Bragg peak—the point of maximal energy deposition—to be positioned within the tumor volume while substantially reducing the dose imparted to adjacent healthy tissues.

The Bragg peak is even narrower for helium and carbon ions than for protons (Figure 1), suggesting that helium- and carbon-ion therapy may, in principle, provide superior tumor conformity and reduced side effects. As the clinical implementation of these ion species has become feasible, comparative evaluation of different hadron-therapy modalities has emerged as a major research focus. Wickert et al., 2022 reported that the use of helium ions instead of conventional photon IMRT resulted in a significant reduction in the integral dose absorbed by healthy brain tissue ($-45.3\% \pm 15.1\%$). Even when compared to actively scanned protons, helium ions achieved a further relative dose reduction of $-27.2\% \pm 14.4\%$ for critical neuronal structures.

Huang et al., 2022 assessed acute dermatitis as an adverse effect, finding that among patients treated with proton therapy, 16 of 18 developed acute grade I/II dermatitis, whereas only 7 of 20 patients treated with CIRT experienced acute grade I dermatitis.

While heavier ions offer superior tumor control, they also carry higher risks for surrounding healthy tissues due to nuclear fragmentation and higher Linear Energy Transfer (LET). Because the potential damage to healthy tissues is higher for helium and carbon ions, ensuring extreme precision in dose delivery is highly important, therefore highly accurate Relative Stopping Power mapping is even more critical for heavy ion therapy than for proton therapy.

1.2. Imaging for Hadron Therapies

In current clinical practice, treatment planning for hadron therapy is predominantly based on X-ray computed tomography (CT) imaging (Kaiser et al., 2019). While X-ray CT provides electron density information of the irradiated tissues, this information must be converted into relative stopping power (RSP) maps in order to perform dose calculations for charged-particle therapy. This conversion relies on empirical calibration curves and introduces systematic uncertainties due to the fundamentally different interaction mechanisms of photons and hadrons with matter (Ordoñez et al., 2019). Hansen et al., 2015 demonstrated that single-energy X-ray CT leads to an RSP uncertainty of approximately 2.7%, which can be reduced to 0.5–0.9% using dual-energy CT; however, the latter approach is technically more complex and costly and while they can reduce them, image artifacts can still be present with this type of imaging (Borges et al.,

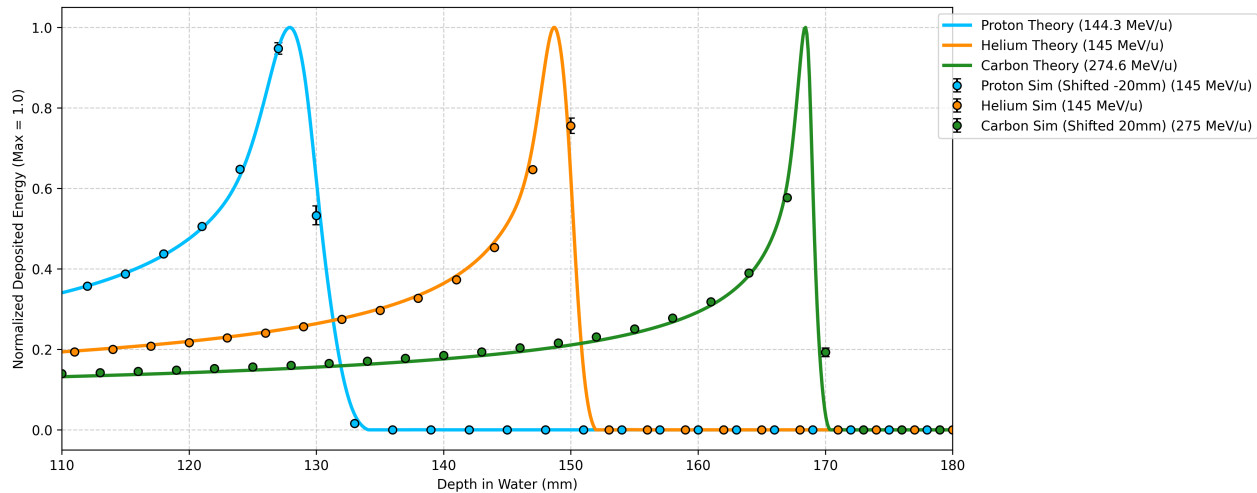


Figure 1: Simulated and fitted Bragg peaks for protons, helium ions and carbon ions. The fit was obtained by integrating over the energies in the Bragg curve (Bragg et al., 1904) sampled from a normal distribution around the most probable energy, accounting for the spread.

2023). These uncertainties translate directly into range errors in hadron therapy, which can reach several millimeters in clinical scenarios and may compromise accurate dose delivery, particularly in regions with heterogeneous tissue composition such as the brain, lungs, or head-and-neck area. Such range uncertainties necessitate the use of additional safety margins, which in turn limit the full exploitation of the steep distal dose fall-off characteristic of hadron beams.

A promising strategy to mitigate these uncertainties is to employ the same type of particle for imaging as for treatment, thereby eliminating the need for photon-to-hadron conversion. In the case of proton therapy, this concept has led to the development of proton computed tomography (pCT), a novel imaging modality that directly reconstructs the RSP distribution of the patient. Recent studies have demonstrated the feasibility of pCT and reported substantial reductions in range uncertainty compared to conventional X-ray CT-based treatment planning, highlighting its strong potential for improving dose accuracy in proton therapy.

As radiotherapy with heavier ions such as helium and carbon gains increasing clinical relevance due to their favorable physical and biological properties, the question naturally arises whether particle imaging with these ions could offer similar or even superior benefits for treatment planning. However, systematic investigations comparing proton-, helium-, and carbon-ion imaging are still limited. Therefore, the objective of this work is to perform a comprehensive comparison of imaging with protons, helium ions, and carbon ions, with particular emphasis on their cumulated dose deposit, their respective imaging performance, achievable range resolution, and potential implications for clinical treatment planning. By evaluating the advantages and limitations of each particle species, this study aims to contribute to the optimization of future image-guided hadron therapy.

2. Methods

2.1. Simulations

For this work, the data taking was done by Monte Carlo simulations, using Geant4 (version 11.0.0) (Agostinelli et al., 2003; Allison et al., 2006) and GATE toolkit (version 9.2) (Jan et al., 2004; Jan et al., 2011) to model the interactions of charged particle beams with a phantom. The setup used in the simulations consisted of a $500 \times 500 \times 100$ mm³ box placed at a longitudinal position of $Z = 400$ mm relative to the world origin. Our motivation is the setup of the Bergen pCT Collaboration (Pettersen et al., 2019; Alme et al., 2020), however for the current study it was not used, instead, a `PhaseSpaceActor` was utilized for the simulations to record the position, direction and energy of the outgoing particles in the phantom.

The simulations utilized the `QGSP_BIC_EMY` physics list to govern hadronic and electromagnetic processes, with the ionization potential of water manually adjusted to 75 eV. The radiation source was modeled as a Pencil Beam Scanning (PBS) system originating at $Z = -500$ mm. To investigate different particle species, three distinct beam configurations were simulated, the protons and the alpha particles maintaining a constant specific energy of 230 MeV/u, while the Carbon-12 ions had 430 MeV/u initial energy. The reason behind the higher energy of the carbon beam is their significantly faster energy loss due to the increased amount of interactions with the electrons of the medium. Since the measurements are comparable only when all Bragg peaks have roughly the same positions, the carbon ion beam needed a higher initial energy than the other two beams. These energies are set to emulate a realistic imaging setup, wherein the Bragg peak would be positioned in the detector, posterior to the patient.

For all cases, the beam was monoenergetic ($\sigma_E = 0.0$ MeV) and characterized by a Gaussian spatial profile with $\sigma_x = \sigma_y = 3$ mm, an angular divergence of 2.8 mrad, and an emittance of 3.0 mm·mrad. The geometrical parameters of the beam also mimic a realistic setup (Giordanengo et al., 2015), however, in the simulations, the authors presupposed an ideal detector system, thus disregarding the uncertainties that would be present in a realistic setup. The effects of these uncertainties are beyond the scope of this study, which focuses exclusively on the advantages and disadvantages of imaging with the aforementioned particles. Phase space data including particle position, direction, and energy were recorded using the previously mentioned `PhaseSpaceActor`.

The simulated phantom used in this study was the CTP404 phantom (The Phantom Laboratory, 2022). This phantom is designed to evaluate the accuracy of material density reconstruction in homogeneous regions. It is a 400 mm long disk with a diameter of 150 mm and contains eight cylindrical rods with a diameter of 12.2 mm, each composed of a different material.

2.2. Dose Calculation

The deposited dose is a key quantity in both particle therapy and imaging applications. To estimate the dose delivered by the investigated particles in a given material, a `DoseActor` was employed in the GATE simulations and attached to the phantom in order to record the deposited energy. The

absorbed dose was calculated according to

$$D = \frac{d\bar{\epsilon}}{dm}, \quad (1)$$

where $d\bar{\epsilon}$ denotes the mean deposited energy and dm the irradiated mass.

The cumulative deposited energy was initially recorded in units of megaelectronvolts and subsequently converted to Joules. The CTP404 phantom is modeled as a cylindrical volume composed primarily of epoxy resin. The dimensions are defined by a radius $r = 75$ mm and a height $h = 400$ mm in order to ensure the offset invariance for this study, giving a total volume of $V \approx 7065.58$ cm³. Assuming a material density of $\rho = 1.16$ g/cm³ (using the `GateMaterials.db` database from the OpenGATE public repository (Jan et al., 2004)), the mass was calculated using density of 1.16 g/cm³.

We performed the simulation scanning the 360° rotation angle in 1° increments and scanning the 155 mm phantom by 1 mm shift increments with 1000 primaries for each setup, and calculated the cumulated dosage.

To ensure a rigorous, unbiased comparison of the dosimetric footprint of each particle species, an identical acquisition framework was utilized across all simulations. This ensures that any variations in the resulting dose and imaging accuracy are strictly attributable to the fundamental physical interactions of the different ions with the medium, rather than discrepancies in particle statistics.

The deposited dose within the CTP404 phantom was calculated using the previously described method. However, because clinical relevance cannot be directly inferred from an epoxy phantom, a first-order analytical scaling model was applied to estimate the equivalent dose for a human head. Based on fundamental dosimetric principles where dose is proportional to deposited energy and inversely proportional to mass ($D = E/m$), the following correction was derived:

$$D_{\text{head}} = D_{\text{phantom}} \times \frac{m_{\text{phantom}}}{m_{\text{head}}} \times \frac{\rho_{\text{head}}}{\rho_{\text{phantom}}} \times \frac{d_{\text{head}}}{d_{\text{phantom}}}. \quad (2)$$

The average mass of the human head was taken as $m_{\text{head}} \approx 4.5$ kg, while the CTP404 phantom's mass was $m_{\text{phantom}} \approx 8.2$ kg. The density correction is based on the Bethe-Bloch formula, which dictates that the mean rate of energy loss is roughly proportional to the density of the absorbing medium ($dE/dx \propto \rho$) (Bethe, 1930). Here, $\rho_{\text{head}} \approx 1.04$ g/cm³ (based on Barber et al., 1970) and $\rho_{\text{phantom}} \approx 1.16$ g/cm³. Finally, the term $d_{\text{head}}/d_{\text{phantom}}$ (where $d_{\text{head}} \approx 16.5$ cm and $d_{\text{phantom}} = 15$ cm) introduces a linear path-length correction analogous to the Size-Specific Dose Estimates (SSDE) methodology outlined in AAPM Report 204 (Boone et al., 2011), adapted here for the linear energy transfer (LET) characteristics of charged particles. Substituting these values yields a scaling factor of 1.814.

2.3. Calculation of RSP Values

The relative stopping power (RSP) values were calculated using GATE10 simulations. Initially, a $1.5 \times 1.5 \times 1.5$ m water cube was simulated, and the Bragg peak positions were determined by identifying the depth at which the maximum energy deposition occurred. The simulations were then repeated for each material comprising the CTP404 phantom. For each material, the RSP was

calculated as the ratio of the water-equivalent path length (WEPL) in water to the WEPL in the given material.

Although the absolute stopping power of ions is highly dependent on their kinetic energy, the RSP normalized to water is essentially energy-independent across the relevant therapeutic or imaging energy range, as demonstrated in Hurley et al., 2012.

Let us denote the path length to the Bragg peak at initial beam energy E as $l(E)$ (often denoted as λ in the literature), and $\overline{\text{SP}}(E, E_p)$ as the *average* Stopping Power value between energies E and E_p , then

$$l(E) \overline{\text{SP}}(E, 0) = l(E_p) \overline{\text{SP}}(E_p, 0) + (l(E) - l(E_p)) \overline{\text{SP}}(E, E_p), \quad (3)$$

where E_p is the beam energy evaluated at a slightly lower value. Hence,

$$\overline{\text{SP}}(E, E_p) = \frac{l(E) \overline{\text{SP}}(E, 0) - l(E_p) \overline{\text{SP}}(E_p, 0)}{l(E) - l(E_p)}. \quad (4)$$

Using $\overline{\text{SP}}(E, 0) = E/l(E)$, we arrive at

$$\overline{\text{SP}}(E, E_p) = \frac{E - E_p}{l(E) - l(E_p)}, \quad \overline{\text{RSP}}(E, E_p) = \frac{\overline{\text{SP}}_{\text{matter}}(E, E_p)}{\overline{\text{SP}}_{\text{water}}(E, E_p)}. \quad (5)$$

To evaluate these equations and accurately determine the energy dependence of the RSP, an analytical fitting approach was applied to the discrete Monte Carlo data. Following standard empirical models, the parameters of the Bragg formula were fitted to the simulated path length–energy dataset using a power-law relationship, $l(E) = b \cdot E^m$. By extracting the material-specific fitting parameters (b and m), the discrete depth-energy data was converted into a continuous function. Subsequently, a uniform energy grid was defined, and the energy dependence of the RSP was calculated by evaluating this fitted $l(E)$ relationship over narrow, symmetric energy steps ($E = E_i + \Delta E$ and $E_p = E_i - \Delta E$, with a step size of $\Delta E = 1$ MeV). This methodology effectively mitigates the statistical fluctuations inherent to the simulated tracks, providing a highly robust calculation of the relative stopping power.

Helium simulations were first employed to validate the calculation method by comparison with known RSP values (Piersimoni et al., 2018). Using 200 MeV/u initial energy, the relative difference between the reference and the simulated RSP values was within 2%.

Following successful validation, the simulations were extended to protons and carbon ions, using the initial energies that were later used for the imaging simulations (230 MeV/u for protons and helium ions, and 430 MeV/u for carbon ions). It is worth noting that the negligible difference between the RSP values is a result of the energy values chosen for the simulations, which allows the Bragg peaks of the different beam types to have roughly the same position. The resulting RSP values for the investigated materials can be seen on Figure 2.

2.4. Image Reconstruction

In particle computed tomography, reconstructing the Relative Stopping Power (RSP) distribution from measured water-equivalent path length (WEPL) values is a complex inverse problem. Various reconstruction strategies have been developed for this purpose, ranging from analytical methods like Filtered Back Projection (FBP) along most likely paths (Rit et al., 2013) to iterative algebraic

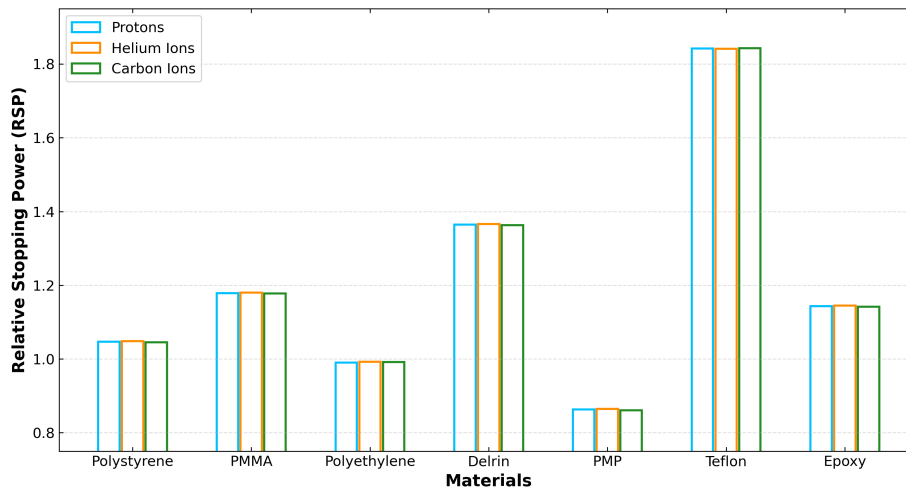


Figure 2: RSP comparison of protons, helium ions and carbon ions, on energies 230 MeV/u, 230 MeV/u and 430 MeV/u for protons, helium ions and carbon ions, respectively. These RSP values are referred to as *ground truth* RSP values later.

techniques such as the Algebraic Reconstruction Technique (ART) or block-iterative methods (Penfold et al., 2010).

However, evaluating or optimizing reconstruction algorithms is beyond the scope of the present study. While several previous studies have investigated the comparative imaging performance of various ion species, our objective here is to strictly assess the intrinsic imaging capabilities of different particle species under identical algorithmic conditions. A detailed comparison of our findings with these existing literature benchmarks is presented in Section 4.2.

To this end, we employed an iterative Richardson–Lucy (RL) deconvolution algorithm, strictly following the mathematical and methodological framework detailed in B  r   et al., 2026.

It is emphasized that this reconstruction algorithm was utilized as a common, baseline processing tool. No particle-specific algorithmic tuning or optimization was performed for the helium and carbon ions, even though the original implementation was not specifically tuned for heavy ions. This approach ensures that any observed differences in image quality and reconstruction accuracy stem directly from the underlying physical interaction properties of the respective particles (such as differences in multiple Coulomb scattering and energy straggling) rather than from software adjustments.

2.5. Evaluation

The quantitative evaluation of the reconstructed RSP distributions was performed using the standard CTP404 phantom. Ground truth (GT) RSP values for the phantom’s material inserts were derived directly from the GATE10 simulations, as described in Section 2.3.

To maintain consistency, the evaluation of reconstruction accuracy followed the exact Region of Interest (ROI) based methodology described in B  r   et al., 2026. By comparing the mean reconstructed RSP values within these predefined ROIs to the GT values, we quantified the material-dependent reconstruction fidelity for protons, helium ions, and carbon ions.

Finally, by synthesizing this RSP accuracy analysis with the previously described dose estimations, we achieved a comprehensive and unbiased comparative evaluation of the imaging performance and dose efficiency of the three particle modalities under identical reconstruction conditions.

3. Results

3.1. Image Reconstruction Accuracy

To evaluate the overall reconstruction accuracy and the evolution of the reconstructed Relative Stopping Power (RSP) distributions, the difference between the ground truth (GT) and the reconstructed maps was first analyzed. Figure 3 presents these difference heatmaps for the entire CTP404 phantom across protons, helium ions, and carbon ions at varying particle statistics. The heatmaps visually demonstrate the progressive reduction in background noise and reconstruction artifacts as the number of processed particles increases towards the final baseline.

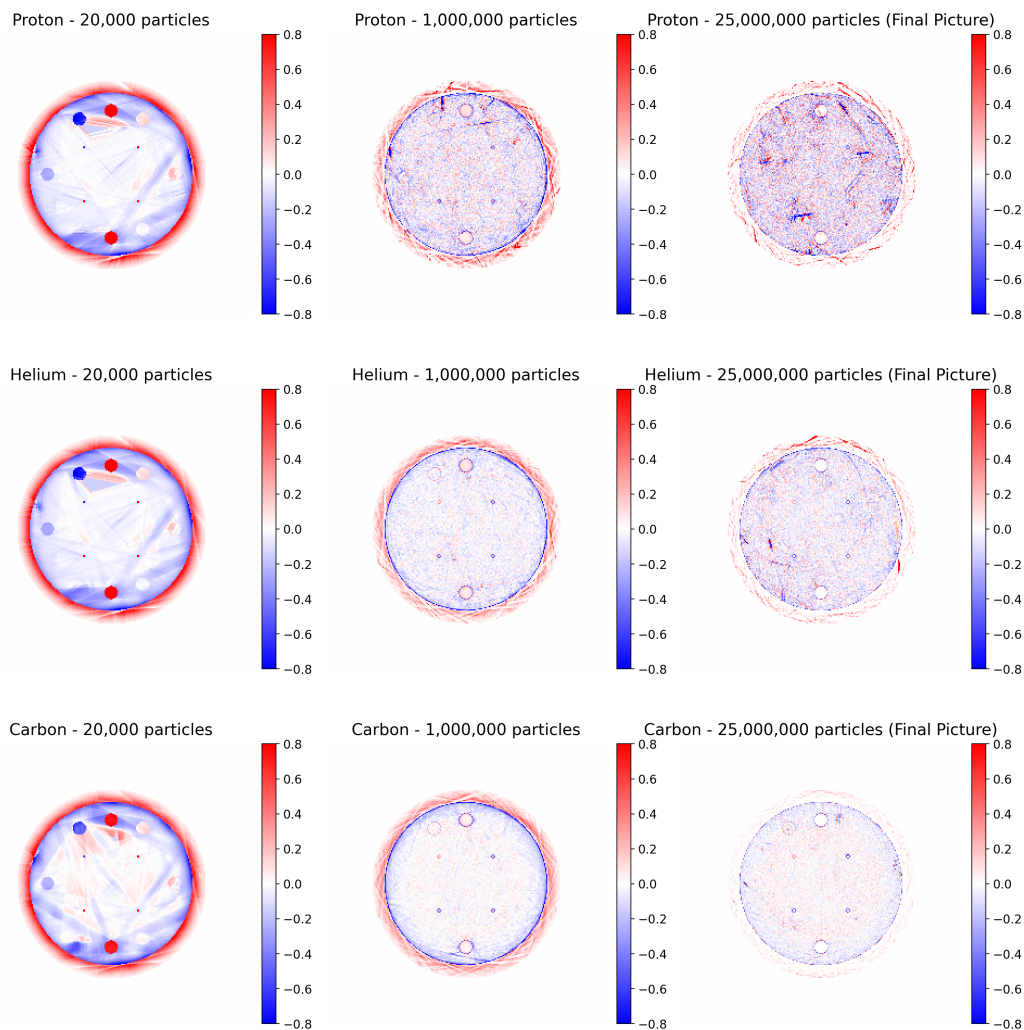


Figure 3: Difference between the ground truth and the reconstruction using different particle numbers.

To more closely examine the material-specific reconstruction fidelity, the visual analysis was narrowed down to the individual material inserts. Figure 4 displays these zoomed-in Regions of Interest (ROIs) for the final reconstructed images of each particle modality. These focused windows allow for a detailed qualitative assessment of the image noise, spatial uniformity, and edge definition within the distinct material cylinders prior to extracting numerical values.

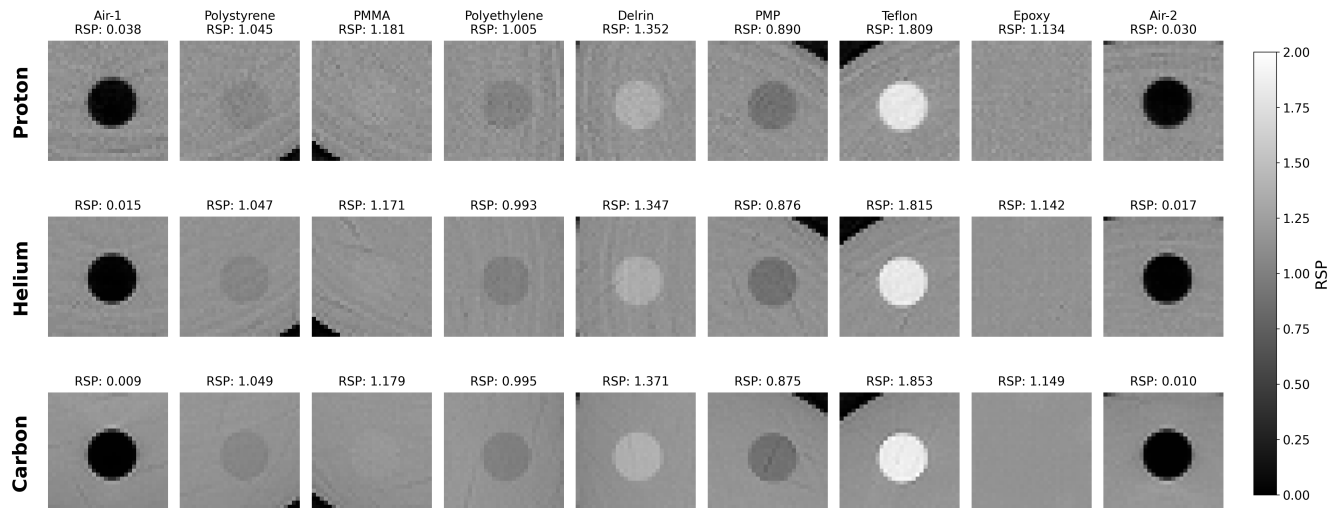


Figure 4: The reconstructed CTP404 inserts using protons, helium ions and carbon ions.

Quantitative evaluation of the imaging performance was conducted by comparing the mean reconstructed RSP values within the regions of interest (ROIs) against the ground truth (GT) values derived from the GATE simulations. The detailed numerical comparison is summarized in Table 1, while the relative differences ($\Delta = (RSP_{\text{rec}} - RSP_{\text{GT}})/RSP_{\text{GT}}$) are illustrated in Figure 5.

Material	Proton		Helium		Carbon	
	GT	Rec.	GT	Rec.	GT	Rec.
Polystyrene	1.047	1.045	1.048	1.047	1.046	1.049
PMMA	1.179	1.181	1.180	1.171	1.177	1.179
Polyethylene	0.990	1.005	0.992	0.993	0.991	0.995
Delrin	1.364	1.352	1.366	1.347	1.363	1.371
PMP	0.863	0.890	0.865	0.876	0.861	0.875
Teflon	1.842	1.809	1.841	1.815	1.843	1.853
Epoxy	1.143	1.134	1.145	1.142	1.142	1.149

Table 1: Comparison of Ground Truth (GT) and Reconstructed (Rec.) RSP values for Protons, Helium ions, and Carbon ions.

The analysis reveals material-dependent deviations characteristic of each particle type:

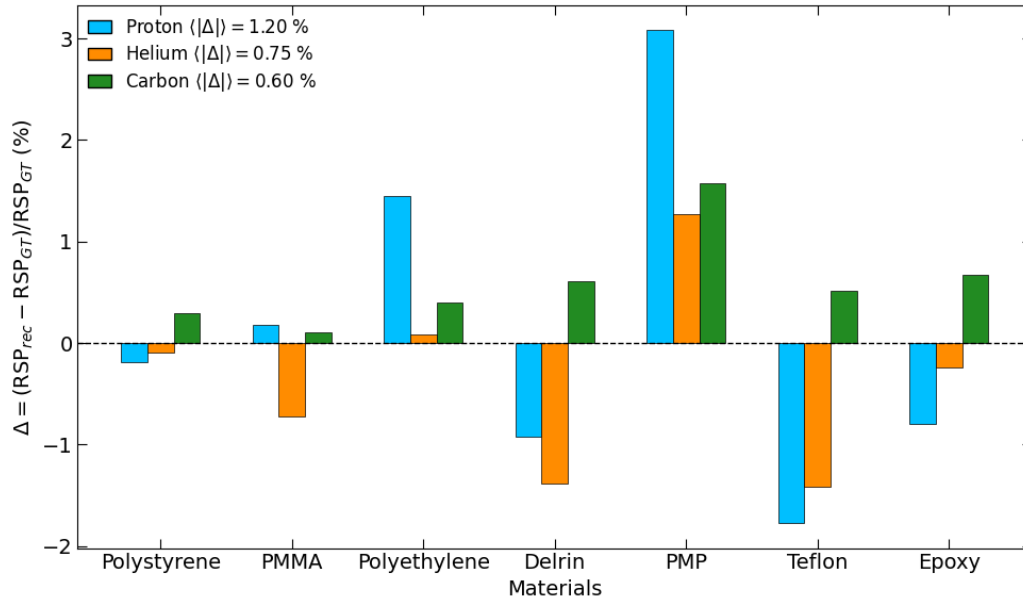


Figure 5: Relative differences between the ground truth and the reconstructed RSP values for all particles. In the legend the mean value of the modulus of the relative difference is indicated.

Protons: Proton imaging demonstrated varying degrees of accuracy across the material spectrum. While reconstruction was exceptionally accurate for intermediate densities—matching the GT of PMMA almost perfectly (+0.2%), larger deviations were observed at the extremes. Specifically, protons exhibited the highest discrepancy for the low-density PMP insert, with an overestimation of approximately +3.1%. A similar trend was observed for Polyethylene, which was overestimated by +1.5%. Conversely, the high-density Teflon insert was substantially underestimated by -1.8% . The mean value of the modulus of the relative difference was 1.2%.

Helium Ions: Helium-based reconstruction showed a general tendency toward underestimation across most materials. Negative deviations were most pronounced for Teflon (-1.4%) and Delrin (-1.4%), as well as for the soft-tissue equivalent material PMMA (-0.8%). However, helium ions performed better than protons in the low-density regime, reconstructing PMP with a much smaller overestimation error of +1.3%. The average of the modulus of the relative difference was also smaller than that of the proton, 0.75%.

Carbon Ions: Carbon ion imaging displayed a highly consistent accuracy profile with a slight overall tendency toward overestimation. It achieved superior accuracy for soft-tissue equivalent materials, particularly PMMA (+0.2%) and Polystyrene (+0.3%). A notable improvement was observed for the high-density Teflon insert; unlike the lighter ions which severely underestimated this material, carbon ions achieved an error of only +0.5% (GT: 1.843, Rec: 1.853). The error for PMP (+1.6%) was significantly lower than that of protons, though slightly higher than helium ions. The mean of the modulus of the relative difference was the smallest for the carbon ions, resulting in 0.60%.

The evaluation of the RSP reconstruction accuracy was also extended to study the dependence on the size of the inserts in the phantom. The simulations were carried out using the previously

described methods, using two modified CTP404 phantoms, where the inserts were 20% smaller and 20% larger. The reconstruction and the evaluation processes were also executed with the aforementioned methods. The differences between the reconstructed RSP values of the modified phantoms and the original one can be seen on Figure 6. For the protons, except for the Polystyrene and the PMMA, an improvement is noticeable with the increasing insert size, however this effect is not present in the case of the helium ions and carbon ions. The difference between the RSP values of the original and the modified phantoms is within 1% on average.

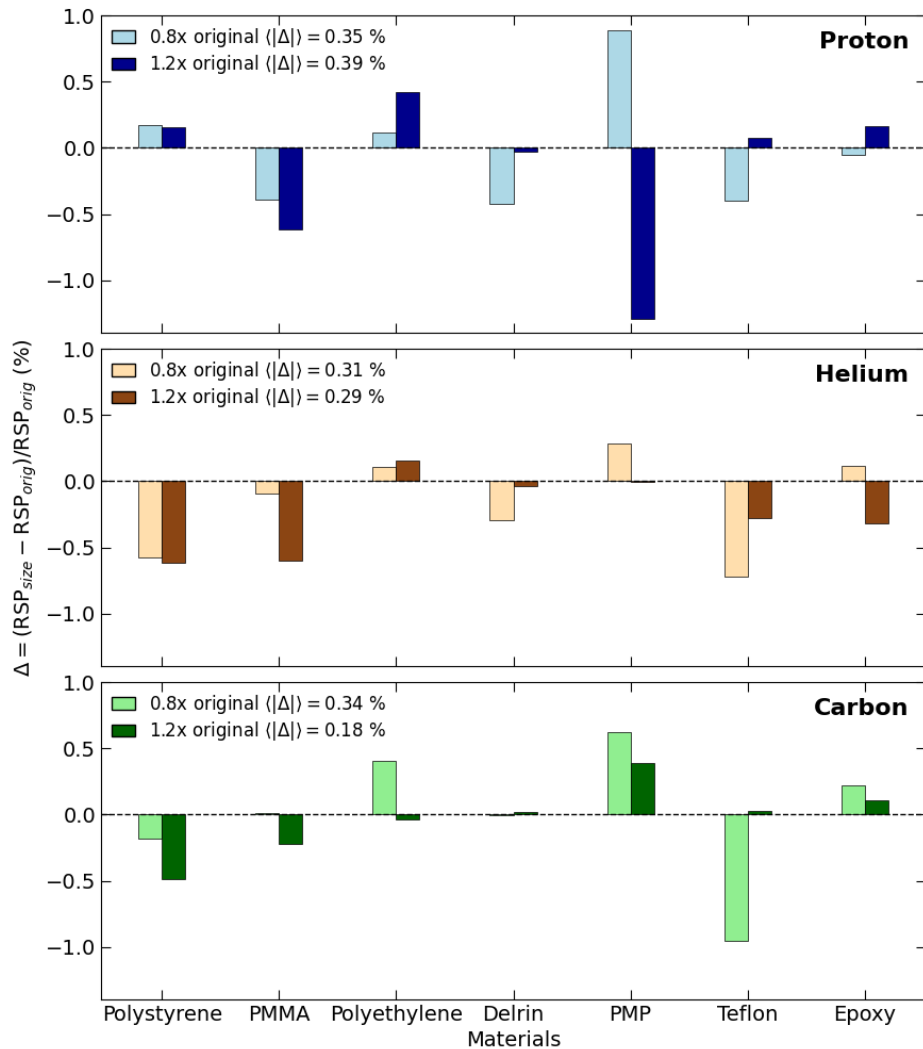


Figure 6: Differences of reconstructed RSP values between the original and the modified sized inserts.

3.2. Convergence and Dose Deposit

The analysis of the reconstruction convergence provides crucial insights into the minimum particle statistics required to achieve stable Relative Stopping Power (RSP) values. Figure 7 illustrates the relative difference between the RSP values at the i -th iteration and the ground truth reconstructed RSP as a function of the number of processed particles.

To evaluate the clinical feasibility of these imaging modalities, the deposited dose corresponding to these convergence thresholds was estimated. Given that deposited dose scales linearly with the number of primary particles, the total baseline dose for a human head (calculated for a full simulation of $360 \times 155 \times 1000 = 55.8 \times 10^6$ primaries) was proportionally recalculated based on the reduced particle counts.

To systematically quantify the stability of the reconstruction, specific convergence thresholds were established. These thresholds are defined by the absolute value of the relative percentage difference ($|\epsilon|$) between the RSP at the i -th iteration and the ground truth reconstructed RSP:

$$|\epsilon| = \left| \frac{\text{RSP}_i - \text{RSP}_{\text{GT}}}{\text{RSP}_{\text{GT}}} \right| \times 100\%. \quad (6)$$

The particle counts required for the reconstruction curve to reach and strictly remain below these defined tolerance windows ($|\epsilon| \leq 1.0\%$, $\leq 0.5\%$, and $\leq 0.25\%$), along with their corresponding optimized human head doses, are detailed in Table 2.

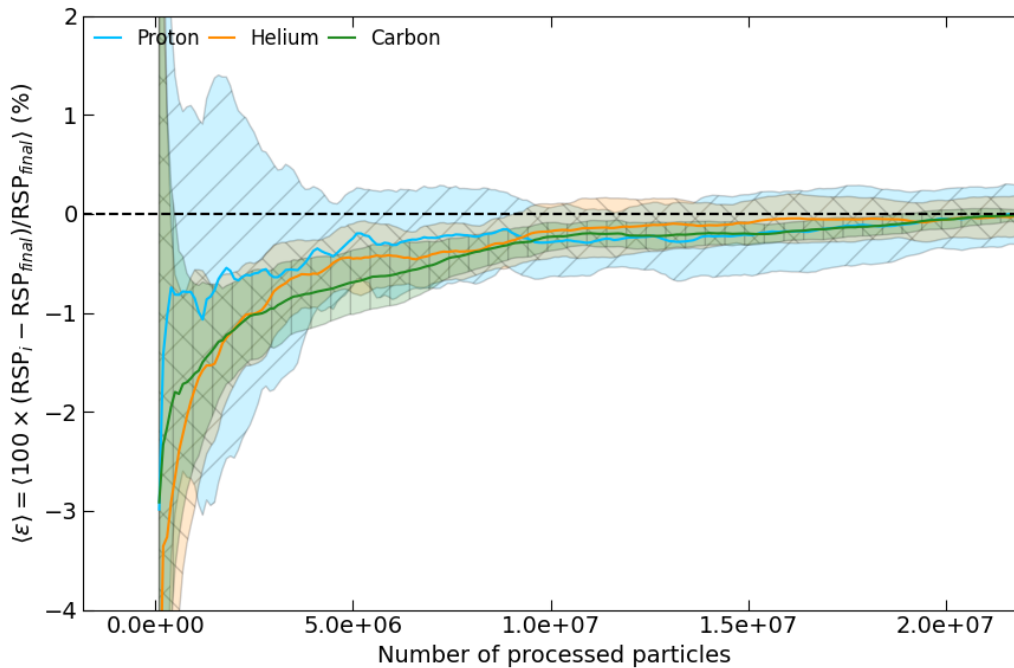


Figure 7: Relative difference between the ground truth reconstructed RSP values and the RSP values in the i -th iteration of the reconstruction as a function of processed particles used for the reconstruction.

The convergence profiles reveal distinct physical behaviors for the different particle species. While protons rapidly reach loose convergence thresholds (requiring only 1.3×10^6 particles to fall

Threshold	Metric	Proton	Helium	Carbon
$\leq 1.0\%$	Required Particles	1,300,000	2,600,000	2,800,000
	Est. Dose (mGy)	0.003	0.022	0.130
$\leq 0.5\%$	Required Particles	3,800,000	4,500,000	7,200,000
	Est. Dose (mGy)	0.009	0.038	0.333
$\leq 0.25\%$	Required Particles	13,800,000	9,200,000	9,800,000
	Est. Dose (mGy)	0.032	0.078	0.454

Table 2: Number of processed particles required to reach and maintain absolute difference convergence thresholds relative to the final reconstructed RSP, alongside the corresponding estimated imaging dose for a human head.

within 1.0% of the final RSP), their convergence curve exhibits significant statistical fluctuation due to higher multiple Coulomb scattering. Consequently, protons require the highest number of particles (13.8×10^6) to fully stabilize within the strict $\leq 0.25\%$ threshold. In contrast, heavier ions display smoother, more monotonic convergence behaviors due to their stiffer particle trajectories. To achieve the high-fidelity $\leq 0.25\%$ threshold, helium and carbon ions require only 9.2×10^6 and 9.8×10^6 particles, respectively. This corresponds to a statistical requirement of approximately 67% and 71% of the particles needed for protons to achieve the same strict stability.

Despite requiring fewer particles for strict convergence, Table 2 demonstrates that carbon and helium ions still deliver a higher absolute dose than protons at the $\leq 0.25\%$ threshold. This escalation in deposited dose is driven by several underlying physical factors. First, according to the Bethe-Bloch equation, electronic stopping power scales with the square of the particle’s effective charge (Z^2). Consequently, heavier ions naturally exhibit a substantially higher linear energy transfer (LET) compared to protons (Schardt et al., 2010). Second, to achieve an equivalent penetration depth in the phantom, the carbon ions required a higher initial kinetic energy (430 MeV/u) compared to the protons and helium ions (230 MeV/u), meaning significantly more total energy was introduced into the system. Finally, unlike protons, heavier ions—particularly carbon—undergo inelastic nuclear collisions as they traverse the medium. This fragmentation process creates a spectrum of lighter, secondary particles (such as protons and alpha particles) that continue to deposit energy even beyond the primary Bragg peak, contributing to a higher integral dose (Gunzert-Marx et al., 2008).

4. Discussion and Comparison

4.1. Dosimetric Performance

One of the most significant findings of this study is the substantial dose reduction offered by particle imaging modalities compared to conventional X-ray computed tomography. As shown in Table 2, the estimated absorbed dose for a human head scan, taking strict reconstruction convergence

requirements into account, can be reduced to as low as 0.032 mGy, 0.078 mGy, and 0.454 mGy, respectively.

Since this study was carried out using a 2-dimensional imaging process, it is worth calculating an estimated dose for a 3-dimensional process, multiplying the 2-dimensional dosage with a given number of slices. To estimate that, we investigated the achievable spatial resolution, which is bounded by the lateral position uncertainty. The calculated lateral spread yielded an intrinsic physical blur of roughly 4 mm, therefore an optimal slice thickness of 4 mm would match the physical resolution limit of the beam. Taking an average human head of 200 mm, the 4 mm slice thickness means 50 slices, resulting in 1.6 mGy, 3.9 mGy and 22.7 mGy for protons, helium ions and carbon ions, respectively.

These values are markedly lower than standard clinical protocols. A typical diagnostic head CT scan delivers an organ absorbed dose to the brain approximately 40 mGy (Huda et al., 2007). Even the carbon-ion scan yielded a dose lower than a standard X-ray CT. The proton and helium scans offer an even more dramatic reduction, potentially lowering the dose by a factor of approximately 10 to over 25 compared to photon-based imaging. It is worth noting that while carbon ions impart a higher physical dose than protons due to their higher Linear Energy Transfer (LET), this is accompanied by reduced multiple Coulomb scattering, which theoretically supports higher spatial resolution (Gehrke et al., 2018).

The results can vary based on the imaging protocol being utilized, however it gives a good estimation and shows that this characteristic could be particularly advantageous for pediatric patients or patients requiring frequent re-imaging for adaptive therapy, where cumulative radiation exposure is a primary concern.

4.2. Comparative Imaging Accuracy

The reconstruction accuracy achieved in this work (typically within 1 – 2%) is consistent with the current state-of-the-art in particle imaging research and compares favorably with X-ray CT benchmarks.

In clinical practice, stoichiometric calibration of single-energy CT (SECT) typically yields RSP uncertainties in the range of 1.6% to 3.5% (Hansen et al., 2015; Yang et al., 2012). Dual-energy CT (DECT) has improved this significantly, achieving accuracies of approximately 0.5% to 1% (Dedes et al., 2019).

Our estimated dose deposits are consistent with the results of Bär et al., 2022, who reported estimated doses of approximately 4.7 mGy and 6.6 mGy for pCT and HeCT, respectively. These values represent a reduction by a factor of 9 compared to SECT and a factor of 13 compared to DECT, maintaining the same order of magnitude as the dosimetric savings observed in our study.

Our results indicate that carbon-ion and helium-ion imaging can achieve RSP accuracy competitive with DECT and superior to SECT, without the need for empirical photon-to-hadron conversion models. While exceptional accuracy was observed for specific tissue-equivalent materials (e.g., approximately 0.2% error for PMMA with carbon ions), the reconstruction remained highly robust across the entire investigated spectrum. For carbon-ion imaging, the relative RSP error was maintained well below 1% for the vast majority of the inserts (ranging between 0.2% and 0.6%), with a maximum deviation of only 1.6% observed for the PMP insert. Similarly, helium-ion

imaging demonstrated consistent precision, keeping relative errors strictly below 1.5% across all materials. This generalized stability across varying densities and compositions strongly underscores the reliable clinical imaging potential of these heavy-ion modalities.

The proton imaging results (errors up to 3.1% for PMP) show slightly higher deviations than the 1 – 2% accuracy reported in some idealized simulation studies (Schulte et al., 2005). This is likely attributable to the simplified Most Likely Path (MLP) formalism used here, which may not fully account for the complex scattering in heterogeneous media compared to more advanced probabilistic solvers. However, our results for helium and carbon ions align well with recent experimental findings. For instance, Gehrke et al. reported helium CT relative range errors of roughly 0.3% to 0.7% (Gehrke et al., 2018), which supports our observation that heavier ions can provide robust reconstruction fidelity.

The observed slight overestimation of Teflon by carbon ions (+0.5%) and substantial underestimation by protons (−1.8%) and helium ions (−1.4%) highlight the non-trivial relationship between particle species and energy loss models in high-density materials. Similar trends have been observed in other Monte Carlo studies, suggesting that nuclear interaction models and ionization potential parameters (I-values) in simulation toolkits (like Geant4) play a critical role in the absolute accuracy of RSP reconstruction (Doolan et al., 2016).

In conclusion, while carbon ions deliver a higher imaging dose than protons or helium, they remain well below the dose burden of conventional X-ray CT while offering superior RSP accuracy and faster statistical convergence for standard tissue-equivalent materials. Helium ions appear to offer a balanced compromise, providing better accuracy than protons (due to reduced scattering) with a dose footprint significantly lower than carbon ions.

5. Summary

In this work, we presented a comprehensive comparative study of proton, helium-ion, and carbon-ion computed tomography (CT) for charged-particle therapy treatment planning. Using high-fidelity Monte Carlo simulations (GATE/Geant4), we evaluated the relative stopping power (RSP) reconstruction accuracy, statistical convergence behavior, and the associated imaging dose for a standard CTP404 phantom.

Our results demonstrate that direct particle imaging offers a viable and potentially superior alternative to conventional X-ray CT for calculating stopping power maps. The key findings are summarized as follows:

Dosimetric Advantage: All three particle imaging modalities demonstrated a substantial reduction in radiation burden compared to standard clinical protocols (~ 40 mGy). When optimized for strict statistical convergence, carbon-ion imaging requires an estimated dose of ~ 22.7 mGy for a human head equivalent. Proton and helium-ion imaging offer further reductions, minimizing the imaging dose to practically negligible levels (~ 1.6 mGy and ~ 3.9 mGy, respectively).

Reconstruction Accuracy: Carbon ions yielded the highest reconstruction fidelity for soft-tissue equivalent materials (e.g., PMMA, Polystyrene) and high-density materials (e.g., Teflon), achieving absolute errors of approximately 0.5% or less. This superior performance is attributed to the reduced multiple Coulomb scattering of heavier ions, which preserves spatial information more

effectively than protons. Helium ions served as an effective compromise, offering better accuracy than protons in low-density regions (such as PMP) while maintaining a significantly lower dose profile than carbon ions. Protons, while delivering the absolute lowest dose, exhibited the highest range of RSP deviations (-1.8% to $+3.1\%$), particularly in materials with extreme densities. The RSP reconstruction accuracy did not show a strong dependence on the insert size, as the difference between the RSP values of the different sized phantoms did not exceed 1% on average.

Statistical Convergence: Heavy ions demonstrated superior spatial stability during the iterative reconstruction process. Carbon and helium ions achieved strict convergence thresholds ($\leq 0.25\%$ absolute difference) requiring approximately 29% and 33% fewer particles than protons, respectively, further validating their efficiency for high-fidelity imaging.

Clinical Implications: The trade-off between image noise, spatial resolution, and patient dose suggests that the optimal particle species may depend on the specific clinical scenario. For pediatric cases or frequent adaptive replanning, proton or helium imaging provides exceptional dose sparing. Conversely, for detailed treatment planning in heterogeneous regions where range accuracy is paramount, carbon-ion imaging offers the highest precision and fastest statistical stability.

Furthermore, this study demonstrates that an algorithm not specifically designed for ion applications can nonetheless perform effective and clinically relevant dose planning using ion beams, provided that accurate ion detection is achieved.

It is worth noting that our study and investigations were executed under idealized circumstances. The results yield a good estimation for the dose deposit and RSP reconstruction accuracy, however future work will focus on validating these simulation results with experimental beam data and investigating the impact of these RSP improvements on the final dose distribution in patient-specific treatment plans.

Acknowledgement

The authors would like to thank the support of the EKÖP-25 University Research Scholarship Program of the Ministry for Culture and Innovation from the source of the National Research, Development and Innovation Fund. Furthermore, the authors acknowledge ELTE Eötvös Loránd University, Budapest, Hungary, as a supporting institution. This work was supported by the Hungarian National Research, Development and Innovation Office (NKFIH) grants under the contract numbers OTKA K135515, 2021-4.1.2-NEMZ_KI-2024-00031, 2021-4.1.2-NEMZ_KI-2024-00033, 2019-2.1.6-NEMZ_KI-2019-00011, 2020-2.1.1-ED-2021-00179, 2022-4.1.2-NEMZ_KI-2022-00009, 2024-1.2.5-TÉT-2024-00022. Computational resources were provided by the Wigner Scientific Computing Laboratory (WSCLAB).

References

Agostinelli, S. et al. (2003). “Geant4—a simulation toolkit”. In: *Nuclear Instruments and Methods in Physics Research Section A: Accelerators, Spectrometers, Detectors and Associated Equipment* 506.3, pp. 250–303. ISSN: 0168-9002. DOI: [https://doi.org/10.1016/S0168-9002\(03\)01368-8](https://doi.org/10.1016/S0168-9002(03)01368-8).

- Allison, J. et al. (2006). “Geant4 developments and applications”. In: *IEEE Transactions on Nuclear Science* 53.1, pp. 270–278. DOI: 10.1109/TNS.2006.869826.
- Alme, J. et al. (2020). “A High-Granularity Digital Tracking Calorimeter Optimized for Proton CT”. In: *Frontiers in Physics* 8. ISSN: 2296-424X. DOI: 10.3389/fphy.2020.568243.
- Barber, Ted W, Judith A Brockway, and Lawrence S Higgins (1970). “The density of tissues in and about the head”. In: *Acta neurologica scandinavica* 46.1, pp. 85–92.
- Bethe, Hans (1930). “Zur theorie des durchgangs schneller korpuskularstrahlen durch materie”. In: *Annalen der Physik* 397.3, pp. 325–400.
- Boone, John et al. (2011). “Size-specific dose estimates (SSDE) in pediatric and adult body CT examinations”. In: (*No Title*).
- Borges, Ana P, Célia Antunes, and Luís Curvo-Semedo (2023). “Pros and cons of dual-energy CT systems: “one does not fit all””. In: *Tomography* 9.1, pp. 195–216.
- Bragg, William Henry and RLXXIV Kleeman (1904). “LXXIV. On the ionization curves of radium”. In: *The London, Edinburgh, and Dublin Philosophical Magazine and Journal of Science* 8.48, pp. 726–738.
- Bär, Esther et al. (2022). “Experimental comparison of photon versus particle computed tomography to predict tissue relative stopping powers”. In: *Medical Physics* 49.1, pp. 474–487. DOI: <https://doi.org/10.1002/mp.15283>. eprint: <https://aapm.onlinelibrary.wiley.com/doi/pdf/10.1002/mp.15283>. URL: <https://aapm.onlinelibrary.wiley.com/doi/abs/10.1002/mp.15283>.
- Bíró, Gábor et al. (2026). *Proton Computed Tomography Image Reconstruction Based on the Richardson-Lucy Algorithm*. arXiv: 2212.00126 [physics.med-ph]. URL: <https://arxiv.org/abs/2212.00126>.
- Dedes, George et al. (2019). “Experimental comparison of proton CT and dual energy x-ray CT for relative stopping power estimation in proton therapy”. In: *Physics in Medicine & Biology* 64.16, p. 165002.
- Doolan, PJ et al. (2016). “Inter-comparison of relative stopping power estimation models for proton therapy”. In: *Physics in Medicine & Biology* 61.22, p. 8085.
- Gehrke, T et al. (2018). “Theoretical and experimental comparison of proton and helium-beam radiography using silicon pixel detectors”. In: *Physics in Medicine & Biology* 63.3, p. 035037.
- Giordanengo, Simona et al. (2015). “The CNAO dose delivery system for modulated scanning ion beam radiotherapy”. In: *Medical physics* 42.1, pp. 263–275.
- Gunzert-Marx, K et al. (2008). “Secondary beam fragments produced by 200 MeV u- 1 12C ions in water and their dose contributions in carbon ion radiotherapy”. In: *New journal of physics* 10.7, p. 075003.
- Hansen, David C et al. (2015). “A simulation study on proton computed tomography (CT) stopping power accuracy using dual energy CT scans as benchmark”. In: *Acta oncologica* 54.9, pp. 1638–1642.
- Huang, Qingting et al. (2022). “Comparison of the efficacy and toxicity of postoperative proton versus carbon ion radiotherapy for head and neck cancers”. In: *Annals of Translational Medicine* 10.22, p. 1197.

- Huda, Walter and Awais Vance (2007). “Patient radiation doses from adult and pediatric CT”. In: *American Journal of Roentgenology* 188.2, pp. 540–546.
- Hurley, RF et al. (2012). “Water-equivalent path length calibration of a prototype proton CT scanner”. In: *Medical physics* 39.5, pp. 2438–2446.
- Jan, S. et al. (2004). “GATE: a simulation toolkit for PET and SPECT”. In: *Physics in Medicine and Biology* 2004-sep 10 vol. 49 iss. 19 49 (19). DOI: 10.1088/0031-9155/49/19/007.
- Jan, S. et al. (2011). “GATE V6: a major enhancement of the GATE simulation platform enabling modelling of CT and radiotherapy”. In: *Physics in Medicine and Biology* 2011-jan 20 vol. 56 iss. 4 56 (4). DOI: 10.1088/0031-9155/56/4/001.
- Kaiser, Adeel et al. (2019). “Proton therapy delivery and its clinical application in select solid tumor malignancies”. In: *Journal of Visualized Experiments (JoVE)* 144, e58372.
- Ordoñez, Caesar E et al. (2019). “Fast in situ image reconstruction for proton radiography”. In: *Journal of radiation oncology* 8.2, pp. 185–198.
- Penfold, Scott N et al. (2010). “Block-iterative and string-averaging projection algorithms in proton computed tomography image reconstruction”. In: *Biomedical Mathematics: Promising Directions in Imaging, Therapy Planning and Inverse Problems*, pp. 347–367.
- Pettersen, H. E. S. et al. (2019). “Design optimization of a pixel-based range telescope for proton computed tomography”. In: *Physica Medica* 63, pp. 87–97. ISSN: 1120-1797. DOI: <https://doi.org/10.1016/j.ejmp.2019.05.026>.
- Piersimoni, Pierluigi et al. (2018). “Helium CT: Monte Carlo simulation results for an ideal source and detector with comparison to proton CT”. In: *Medical physics* 45.7, pp. 3264–3274.
- Rit, Simon et al. (2013). “Filtered backprojection proton CT reconstruction along most likely paths”. In: *Medical physics* 40.3, p. 031103.
- Schardt, Dieter, Thilo Elsässer, and Daniela Schulz-Ertner (2010). “Heavy-ion tumor therapy: Physical and radiobiological benefits”. In: *Reviews of modern physics* 82.1, pp. 383–425.
- Schulte, Reinhard W et al. (2005). “Density resolution of proton computed tomography”. In: *Medical physics* 32.4, pp. 1035–1046.
- The Phantom Laboratory (2022). *Catphan® 600 phantom (containing CTP404 and CTP528 as a section)*. Last accessed 5 October 2022. URL: <https://www.phantomlab.com/catphan-600>.
- Wickert, Ricarda et al. (2022). “Radiotherapy with Helium ions has the potential to Improve both Endocrine and Neurocognitive Outcome in Pediatric patients with Ependymoma”. In: *Cancers* 14.23, p. 5865.
- Yang, Ming et al. (2012). “Comprehensive analysis of proton range uncertainties related to patient stopping-power-ratio estimation using the stoichiometric calibration”. In: *Physics in Medicine & Biology* 57.13, p. 4095.